ChemPhysChem

Articles
doi.org/10.1002/cphc.202100032

**Chemistry
Europe**
European Chemical
Societies Publishing

Phase-field Determination of NaSICON Materials in the Quaternary System Na$_2$O–P$_2$O$_5$–SiO$_2$–ZrO$_2$: The Series Na$_3$Zr$_{3-x}$Si$_2$P$_x$O$_{11.5+x/2}$

A. Loutati,[a, b] Y. J. Sohn,[a] and F. Tietz*[a, b]

Two types of solid electrolytes have reached technological relevance in the field of sodium batteries: ß/ß''-aluminas and NaSICON-type materials. Today, significant attention is paid to room-temperature stationary electricity storage technologies and all-solid-state Na batteries used in combination with these solid electrolytes are an emerging research field besides sodium-ion batteries. In comparison, NaSICON materials can be processed at lower sintering temperatures than the ß/ß''-aluminas and have a similarly attractive ionic conductivity. Since Na$_2$O–SiO$_2$–ZrO$_2$–P$_2$O$_5$ ceramics offer wider compositional variability, the series Na$_3$Zr$_{3-x}$Si$_2$P$_x$O$_{11.5+x/2}$ with seven compositions ($0 \leq x \leq 3$) was selected from the quasi-quaternary phase diagram in order to identify the predominant stability region of NaSICON within this series and to explore the full potential of such materials, including the original NaSICON composition of Na$_3$Zr$_2$Si$_2$PO$_{12}$ as a reference. Several characterization techniques were used for the purpose of better understanding the relation-ships between processing and properties of the ceramics. X-ray diffraction analysis revealed that the phase region of NaSICON materials is larger than expected. Moreover, new ceramic NaSICON materials were discovered in the system crystallizing with a monoclinic NaSICON structure (space group *C2/c*). Impedance spectroscopy was utilized to investigate the ionic conductivity, giving clear evidence for a dependence on crystal symmetry. The monoclinic NaSICON structure showed the highest ionic conductivity with an optimum ionic conductivity of 1.22×10^{-3} at 25 °C for the composition Na$_3$Zr$_2$Si$_2$PO$_{12}$. As the degree of P^{5+} content increases, the total ionic conductivity is initially enhanced until $x = 1$ and then decreases again. Simultaneously, the increasing amount of phosphorus leads a decrease in the sintering temperatures for all samples, which was confirmed by dilatometry measurements. The thermal and microstructural properties of the prepared samples are also evaluated and discussed.

1. Introduction

Lithium-ion batteries with high energy density, long cycle life and good performance have attracted worldwide attention since their commercialization by Sony in 1990 and are the main energy storage systems in several market segments.[1] However, the large-scale demand for lithium metal brings up other issues, such as the limited easily accessible sources of lithium salts. Hence, these lithium resources might not meet the increasing demand for energy storage capacity.[2] In order to potentially supplement the storage supply, especially for stationary energy storage, sodium has been considered due to its inexpensive and very abundant salts.[3,4] Since the electrolyte is an indis-

pensable and central part of batteries, the investigation and optimization of suitable liquid and solid electrolyte materials are crucial for the development of Na-ion batteries (NIBs) and Na-solid-state batteries, respectively. In the case of solid electro-lytes, development during recent decades was dominated by the β/β''-aluminas and batteries with these electrolytes have already been commercialized. The total ionic conductivity of β/β''-alumina ceramics can reach up to 6×10^{-3} S cm^{-1} at room temperature.[5,6] At the same time, materials with a kosnarite structure[7] and initially called Na$^+$ super ionic conductors (NaSICONs)[8,9] have been intensively studied. Recently, the solid solution Na$_{3+x}$Zr$_2$(SiO$_4$)$_{2+x}$(PO$_4$)$_{1-x}$ was re-investigated and the best total conductivity of a NaSICON material was determined to be 5.2×10^{-3} S cm^{-1} for $x = 0.4$.[10] For both types of materials, a wide variety of novel batteries are under development today for operation temperatures ranging from 200 °C down to below room temperature.[11] The NaSICONs are very promising materi-als, because they usually can be processed into ceramic components at lower temperatures than the β/β''-aluminas.

During the past four decades, mainly the series Na$_{1+x}$Zr$_2$(SiO$_4$)$_x$(PO$_4$)$_{3-x}$ has been extensively characterized. However, the existence of NaSICON materials is not restricted to this solid solution. In the Na$_2$O–P$_2$O$_5$–SiO$_2$–ZrO$_2$ system, the NaSICON stability region in the phase diagram can be regarded as a compressed tetrahedron based on the solid solutions that define the edges of this tetrahedron.[12] However, compositions also exist outside this tetrahedron, but they still crystallize in a

[a]   A. Loutati, Dr. Y. J. Sohn, Dr. F. Tietz
      Institute of Energy and Climate Research, Materials Synthesis and
      Processing (IEK-1)
      Forschungszentrum Jülich GmbH
      52425 Jülich, Germany
      E-mail: f.tietz@fz-juelich.de
[b]   A. Loutati, Dr. F. Tietz
      Helmholtz Institute Münster: Ionics in Energy Storage (IEK-12)
      Forschungszentrum Jülich GmbH
      52425 Jülich, Germany

kosnarite or NaSICON structure[13] and were formerly also named "TITZICON".[14,15]

NaSICON-type compounds are associated with their crystal structure and are based on the general formula $AB_2(PO_4)_3$. The structure is composed of corner-sharing PO_4 tetrahedra and BO_6 octahedra, providing an open 3D network of sites and conduction pathways for various A cations. In general, the materials crystallize with rhombohedral symmetry (space group $R\bar{3}c$). However, depending on the composition, the rhombohedral structure can undergo a monoclinic distortion (space group $C2/c$), as is the case for the series $Na_{1+x}Zr_2(SiO_4)_x(PO4)_{3-x}$ with $1.8 \leq x \leq 2.2$.[9] In the rhombohedral crystal structure two sites are preferentially occupied by Na^+ ions: a sixfold-coordinated site with three oxygen ions of three $(Si,P)O_4$ tetrahedra above and below (Wyckoff position $6b$ at (0, 0, 0); Na(1)) and an eightfold-coordinated site (Wyckoff position $18e$ (x, 0, 0.25); Na(2)).[9,16] The monoclinic distortion allows the occupancy of a third sodium site. The Na(3) sites are sixfold-coordinated to oxygen ions of three ZrO_6 octahedra.[17] The conduction occurs by hopping from the Na(1) to the Na(2) or Na(3) sites through oxygen triangles with a hopping distance of approximately 3 Å depending on the composition and lattice parameters of each material.
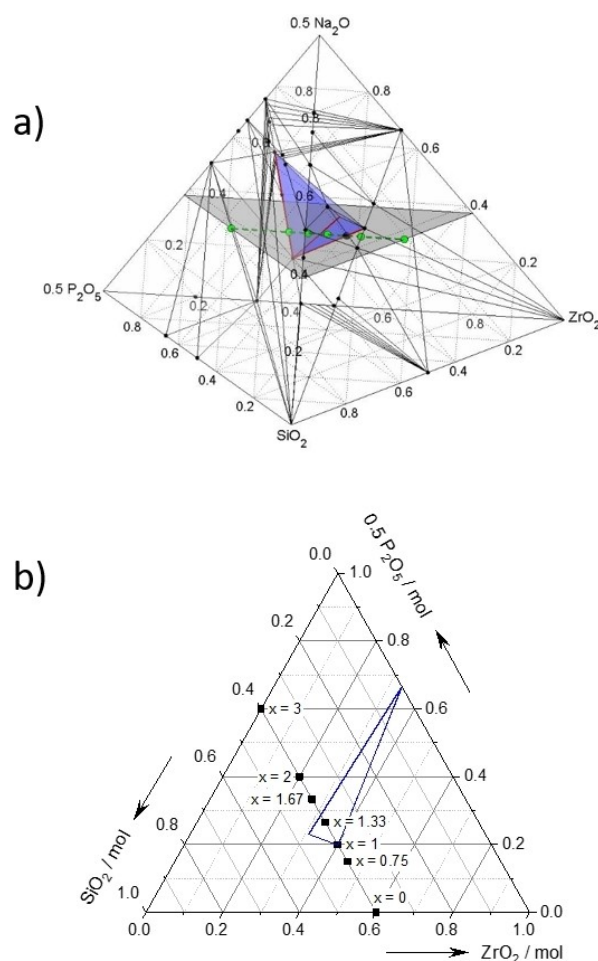
This work is the beginning of a more general exploration of the quaternary phase diagram Na_2O–SiO_2–ZrO_2–P_2O_5 to identify the real phase stability region of NaSICON materials. However, it should be noted that these investigations are not purely thermodynamics-oriented in the sense that phase analyses are not carried out at a constant temperature and pressure. Instead, the investigations are materials-science-oriented with the aim of identifying appropriate processing parameters for the determination of physical properties of interest, like the ionic conductivity of the materials.

Here the series $Na_3Zr_{3-x}Si_2P_xO_{11.5+x/2}$ with seven compositions ($0 \leq x \leq 3$) was selected from the quaternary phase diagram including the original NaSICON composition $Na_3Zr_2Si_2PO_{12}$.[8,9] as an internal reference (Figure 1). The thermal, microstructural, crystallographic and electrical properties of the prepared samples are evaluated and discussed.

Figure 1. a) The quaternary phase diagram Na_2O–SiO_2–ZrO_2–P_2O_5 visualizing the position of the nominal series $Na_3Zr_{3-x}Si_2P_xO_{11.5+x/2}$ with $x=0$, 0.75, 1, 1.33, 1.67, 2 and 3 (from right to left) shown as green circles ($Na_3Zr_2Si_2PO_{12}$ in dark green). The grey plane indicates compounds with a constant molar fraction of $\xi_{Na}=0.375$. The blue compressed tetrahedron corresponds to the phase field of NaSICON materials (see [12] for further details). **b)** Ternary plot of the grey plane in Figure 1a. The blue lines indicate the cross section of the NaSICON tetrahedron at $\xi_{Na}=0.375$. According to this graph, only the series members with $x=1$ and $x=1.33$ can be ascribed to the phase field of NaSICON.

2. Results and Discussion

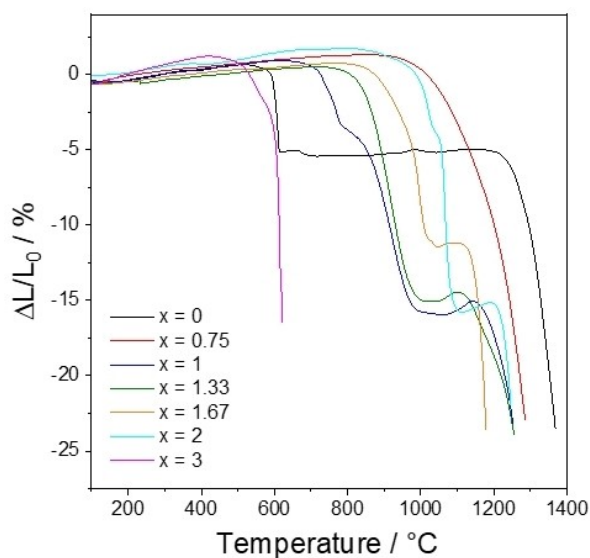### 2.1. Dilatometry and Sintering Experiments

The shrinkage behavior of the pellets was recorded with dilatometry to identify the optimal sintering temperature of all compositions. The shrinkage was measured during constant heating until a shrinkage of 25% was reached (Figure 2). The shrinkage value of 25% already exceeds the theoretical value of 20.6% that is necessary to obtain full density for a typical pellet with a diameter of 8 mm, a thickness of 5 mm and an initial density of 50%. At this shrinkage level it can be assumed that, towards the end of the measurement, a further increase in temperature either leads to the melting of the sample or to a continuous plastic deformation of the specimen induced by the low pressure of the push-rod.

Apart from the sample with $x=0.75$, a multiple step shrinkage behavior is observed. In the case of $Na_3Zr_3Si_2O_{11.5}$, the pellet sharply shrinks at 600 °C, suggesting that partial melting occurs. Recrystallization is then observed, and a second shrinkage starts at about 1220 °C with the highest shrinkage rate at 1360 °C.

The pellets of the compositions $Na_3Zr_2Si_2PO_{12}$, $Na_3Zr_{1.67}Si_2P_{1.33}O_{12.17}$ and $Na_3Zr_{1.33}Si_2P_{1.67}O_{12.33}$ show three sintering processes and shrink up to about 1230 °C, with a relative density of 96%, 93% and 92%, respectively, thus remaining good-quality ceramics. In a temperature region of about 100–200 °C before the third sintering step, an intermediate crystallization with a small volume increase is observed. $Na_3ZrSi_2P_2O_{12.5}$ behaves very similarly, but only two sintering processes can be distinguished. $Na_3Si_2P_3O_{13}$ has a very narrow temperature region for sintering and melts at 600 °C.

ChemPhysChem

Articles
doi.org/10.1002/cphc.202100032

**Chemistry
Europe**

European Chemical
Societies Publishing

Figure 2. Sintering curves of $Na_3Zr_{3-x}Si_2P_xO_{11.5+x/2}$ samples with a constant heating rate up to 1400 °C.
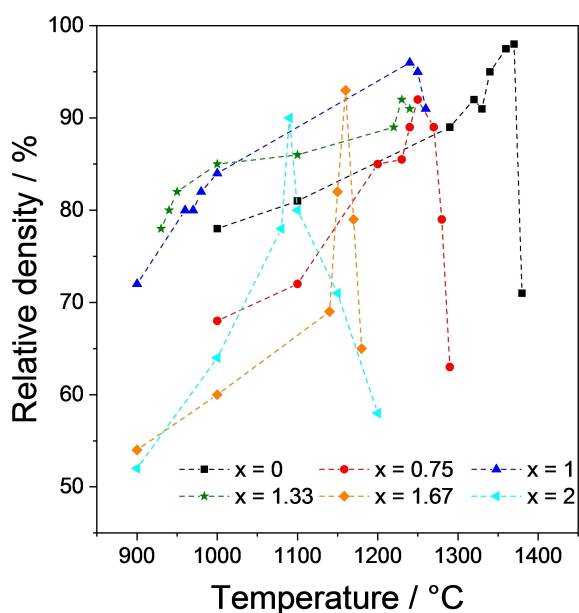
Figure 3. Relative densities obtained at different sintering temperatures.

Table 1. Sintering temperature (T_s), shrinkage and resulting densities of the $Na_3Zr_{3-x}Si_2P_xO_{11.5+x/2}$ compounds.

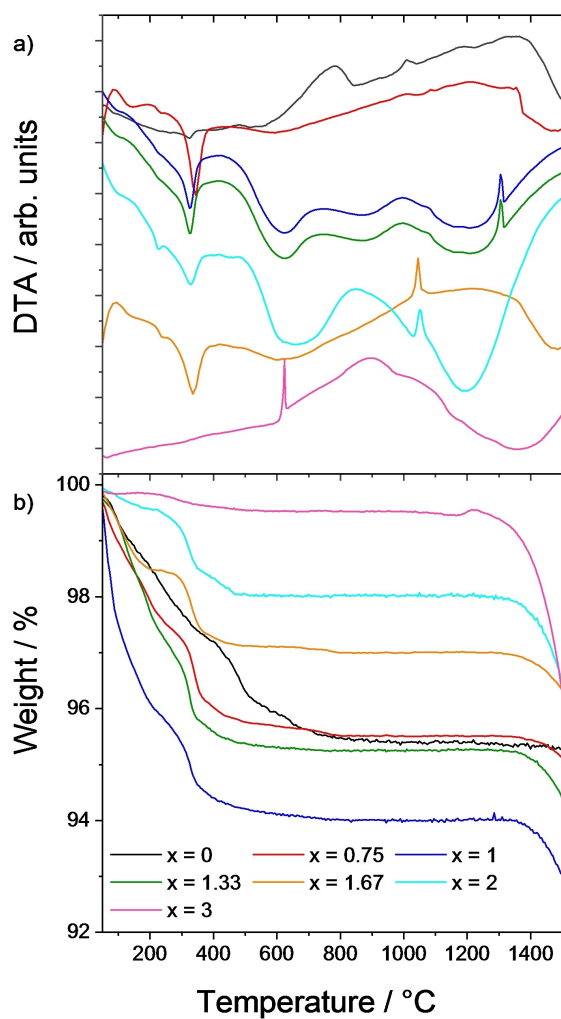| Composition	T_s/°C	Linear shrinkage in dilatometer/ %	Volume shrinkage in furnace/%	Relative density/ %
$Na_3Zr_3Si_2O_{11.5}$	1370	23	21.5	98
$Na_3Zr_{2.25}Si_2P_{0.75}O_{11.87}$	1250	16	12	94
$Na_3Zr_2Si_2PO_{12}$	1240	20	14	96
$Na_3Zr_{1.67}Si_2P_{1.33}O_{12.17}$	1230	25	14.3	93
$Na_3Zr_{1.33}Si_2P_{1.67}O_{12.33}$	1160	18	12.6	92
$Na_3ZrSi_2P_2O_{12.5}$	1060	19	15.2	90
$Na_3Si_2P_3O_{13}$	600	4	2.3	59

To achieve an optimal sintering of each composition, the pressed cylindrical pellets were sintered at different temperatures, at which the shrinkage in the dilatometer curves varied between 10 % ($T_{10\%}$) and 25 % ($T_{25\%}$). The sintering experiments in the furnace were carried out between $T_{10\%}$ and $T_{25\%}$ in steps of 10 °C for three hours in air. In this way, the ideal sintering temperature for each composition was obtained. The resulting densities of the different sintering experiments are shown in Figure 3. Table 1 summarizes the highest densities achieved for each composition.

The dilatometer measurement as well as the sintering experiments in the furnace revealed a systematic decrease of the sintering temperature with increasing phosphorus content. The reason behind this trend is the glass phase formation in the ZrO_2-poor region of the quaternary phase diagram. Especially in the ternary Na_2O–SiO_2–P_2O_5 system, a large number of low melting compounds exist[12] with a vast number of eutectic and peritectic points. In the special case of $Na_3Si_2P_3O_{13}$, this composition lies exactly on the conoidal line of SiO_2 and $NaPO_3$, the latter with a melting point of 588 °C.[18] These results are in accordance with DTA/TG measurements as will be discussed in the next section.

The reduced sintering temperatures of 1060 °C and 1160 °C for the compositions $Na_3ZrSi_2P_2O_{12.5}$ and $Na_3Zr_{1.33}Si_2P_{1.67}O_{12.33}$, respectively, can also be linked to existing neighboring phases such as $Na_4P_2O_7$ and $Na_5Si_2PO_9$ with melting points below 1000 °C.[19] This reduction of sintering temperature has a significant impact on the temperature window in which the densification process can be optimized. At reduced sintering temperatures, the temperature region between enhanced sintering shrinkage and melting can be as narrow as 10 °C, resulting in difficulties in adjusting the proper sintering temperature.

2.2. Thermal Analysis

DTA/TG measurements were carried out up to 1500 °C to analyze the formation and stability of the crystalline phase, to quantify mass losses and to identify the melting points. The TG curves show two temperature domains with weight losses (Figure 4). The first weight loss appears in the temperature range from room temperature up to 500 °C and can be attributed to the volatilization of CO_2 and the release of the crystal water contained in the materials. The second weight loss starts between 1200 °C and 1300 °C and is ascribed to the evaporation of sodium oxide and phosphorus pentoxide from the material.[18] The evaporation is pronounced when the materials are already partially molten. Therefore, the nearly flat line of $Na_3Zr_3Si_2O_{11.5}$ between 1200 °C and 1500 °C should not be regarded as a measurement without weight loss. A careful analysis of the TG curve showed a low evaporation rate of 0.3 %/h (i.e. 0.046 mg/h) due to the absence of phosphorus and a persisting solid up to the end of the measurement. Instead, for $Na_3Zr_2Si_2PO_{12}$ an evaporation rate of 4.5 %/h (i.e. 1.5 mg/h) can be derived at the end of the measurement, which is a

ChemPhysChem

Articles
doi.org/10.1002/cphc.202100032

**Chemistry
Europe**
European Chemical
Societies Publishing

Figure 4. Thermal investigation of the series $Na_3Zr_{3-x}Si_2P_xO_{11.5+x/2}$: **a)** DTA results, and **b)** TG results.

Table 2. Melting points determined by sintering experiments in the furnace and by optical inspection (TOMMI plus). The weight loss during DTA/TG measurements of $Na_3Zr_{3-x}Si_2P_xO_{11.5+x/2}$ refers to the high-temperature interval between 1000 °C and 1500 °C.

Composition	Melting temperature/°C	Melting point/°C (Tommy+)	Weight loss/%
$Na_3Zr_3Si_2O_{11.5}$	1385	1400 ± 20	0.13
$Na_3Zr_{2.25}Si_2P_{0.75}O_{11.87}$	1290	1282 ± 10	0.42
$Na_3Zr_2Si_2PO_{12}$	1280	1280 ± 10	0.96
$Na_3Zr_{1.67}Si_2P_{1.33}O_{12.17}$	1260	1270 ± 10	0.85
$Na_3Zr_{1.33}Si_2P_{1.67}O_{12.33}$	1180	1190 ± 10	0.67
$Na_3ZrSi_2P_2O_{12.5}$	1100	1260 ± 20	1.59
$Na_3Si_2P_3O_{13}$	620	627 ± 10	3.28

2.3. Chemical Analysis

The compositions of the investigated powders and ceramic specimens were chemically analyzed to control their accurate stoichiometry and the ICP-OES results are summarized in Table 3. The obtained atomic ratios were normalized to 2 mol silicon per formula unit. The stoichiometry of the compounds showed that the addition of phosphorus and the reduction of zirconium was successful with good precision. Before sintering, the sodium content was slightly higher to compensate the possible loss of sodium oxide during sintering. However, after sintering the sodium content was found to be lower than expected for all compositions, which is due to weight losses during sintering[19,20] as mentioned before. Figure 5 reveals that a systematic sodium loss is observed with increasing zirconium content, which at first seems to be surprising. However, the amount of weight loss was very high in the case of $Na_3Zr_3Si_2O_{11.5}$ because of the sintering process at a high temperature (1370 °C), whereas $Na_3Si_2P_3O_{13}$ was sintered at a low temperature (600 °C). As a result, the weight loss was negligible in the latter case. This result highlights once again the impact of the high sintering temperature on the loss of sodium oxide, which is difficult to re-adjust. The concentration of zirconium and silicon is in good agreement with the nominal composition. Almost no phosphorus pentoxide evaporation was observed, and the achieved phosphorus concentration was close to the anticipated values. The amount of oxygen per formula unit was not determined experimentally.

representative evaporation rate for the other members of the series.

In the DTA curves, sharp endothermic signals are observed between 1000 °C and 1300 °C for the samples with $0.75 \leq x \leq 2$. The signals at about 1000 °C for $x = 1.67$ and $x = 2$ coincide with the strong shrinkage during the dilatometer measurements and can be ascribed to partial melting or amorphization in the materials. In the other samples with $x = 0.75$ and $x = 1$, the signals close to 1300 °C can be clearly ascribed to the complete melting of the ceramics in combination with the XRD results discussed below. The sharp endothermic signal detected with $Na_3Si_2P_3O_{13}$ at 624 °C with an onset at 616 °C is in very good agreement with the dilatometric detection of the melting point.

The melting temperatures of the compounds in the series $Na_3Zr_{3-x}Si_2P_xO_{11.5+x/2}$ were also measured with a thermo-optical device and are listed in Table 2.

Table 3. Composition of the $Na_3Zr_{3-x}Si_2P_xO_{11.5+x/2}$ compounds determined by ICP-OES and normalized to 2 mol silicon per formula unit. The experimental error varied between 3% and 8%. The oxygen content was calculated on the basis of the cation contents.

Nominal composition	Analytical stoichiometry before sintering	Analytical stoichiometry after sintering
$Na_3Zr_3Si_2O_{11.5}$	$Na_{3.04}Zr_{3.06}Si_2O_{11.6}$	$Na_{2.68}Zr_{3.04}Si_2O_{11.4}$
$Na_3Zr_{2.25}Si_2P_{0.75}O_{11.87}$	$Na_{3.02}Zr_{2.27}Si_2P_{0.79}O_{12.0}$	$Na_{2.75}Zr_{2.21}Si_2P_{0.77}O_{11.7}$
$Na_3Zr_2Si_2PO_{12}$	$Na_{3.02}Zr_{2.10}Si_2P_{1.08}O_{12.4}$	$Na_{2.79}Zr_{2.06}Si_2P_{1.02}O_{12.1}$
$Na_3Zr_{1.67}Si_2P_{1.33}O_{12.17}$	$Na_{3.05}Zr_{1.66}Si_2P_{1.41}O_{12.4}$	$Na_{2.82}Zr_{1.65}Si_2P_{1.28}O_{11.9}$
$Na_3Zr_{1.33}Si_2P_{1.67}O_{12.33}$	$Na_{3.06}Zr_{1.34}Si_2P_{1.58}O_{12.2}$	$Na_{2.91}Zr_{1.33}Si_2P_{1.51}O_{11.9}$
$Na_3ZrSi_2P_2O_{12.5}$	$Na_{3.04}Zr_{1.08}Si_2P_{2.04}O_{12.8}$	$Na_{2.95}Zr_{1.04}Si_2P_{2.03}O_{12.6}$
$Na_3Si_2P_3O_{13}$	$Na_{3.06}Si_2P_{3.04}O_{13.1}$	$Na_{2.98}Si_2P_{3.03}O_{13.1}$

ChemPhysChem

Articles
doi.org/10.1002/cphc.202100032

Chemistry
Europe
European Chemical
Societies Publishing
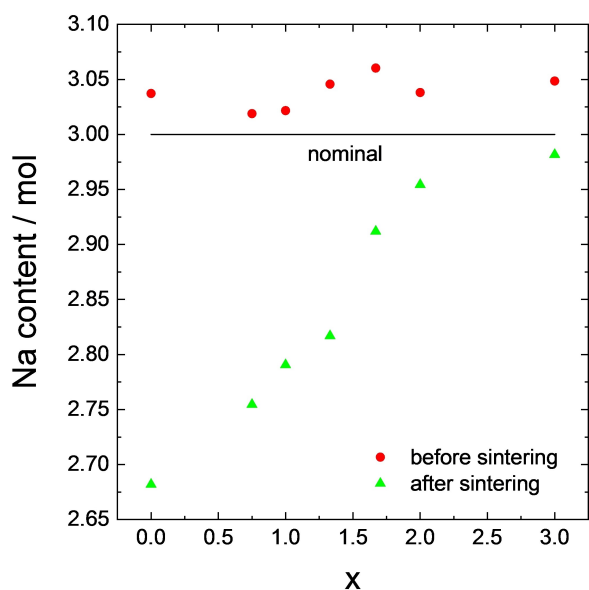
Figure 5. Variation of sodium content in the series $Na_3Zr_{3-x}Si_2P_xO_{11.5+x/2}$ with $0 \leq x \leq 3$ before and after sintering. The results were normalized to 2 mol silicon per formula unit. The pellets were sintered at the temperatures listed in Table 3 for 3 h in air.

2.4. Crystallographic Analysis

2.4.1. Phase Contents

The X-ray diffraction (XRD) patterns of the samples after sintering at optimal temperatures (Table 1) are shown in Figure 6. The samples with $x = 0.75$, 1 and 1.33 crystallized with a monoclinic NaSICON structure (space group $C2/c$),[21] while the other samples with $x = 0$, 1.67 and 2 crystallized with rhombohedral symmetry. To determine the influence of the compositional variation on the NaSICON structure and to identify the amounts of the individual phases, the refinement of the XRD patterns was carried out using Rietveld analysis. The results of the refinements showed rather high amounts of NaSICON phase even for those compositions which are not very close to the phase field of NaSICON (Figure 1).

$Na_3Zr_3Si_2O_{11.5}$ contained 70 wt.% of the $R\bar{3}c$ phase refined as $Na_4Zr_2Si_3O_{12}$ (Inorganic Crystal Structure Database, ICSD No. 15546)[22] and 30 wt.% of monoclinic ZrO_2 with space group $P2_1/c$ (ICSD No. 60900).[23] The sample was sintered at a high sintering temperature of 1370 °C and the significant loss of Na_2O by volatilization above 1230 °C[24] caused an expulsion of Zr^{4+} cations from the NaSICON phase,[25,26] leading to the formation of monoclinic ZrO_2. Boilot et al.[27] and Bayard et al.[28] have also reported the presence of monoclinic ZrO_2 at a high sintering temperature. The nominal composition $Na_3Zr_3Si_2O_{11.5}$ converted to $Na_4Zr_2Si_3O_{12}$ with lattice parameters $a = 9.187(6)$ Å and $c = 22.22(1)$ Å, which are very close to those reported earlier.[23]

Instead, the samples sintered at 1250 °C ($x = 0.75$) and 1240 °C ($x = 1$) exhibit the monoclinic NaSICON phase comparable with $Na_3Zr_2Si_2PO_{12}$ (ICSD No. 202154)[21] and a low content
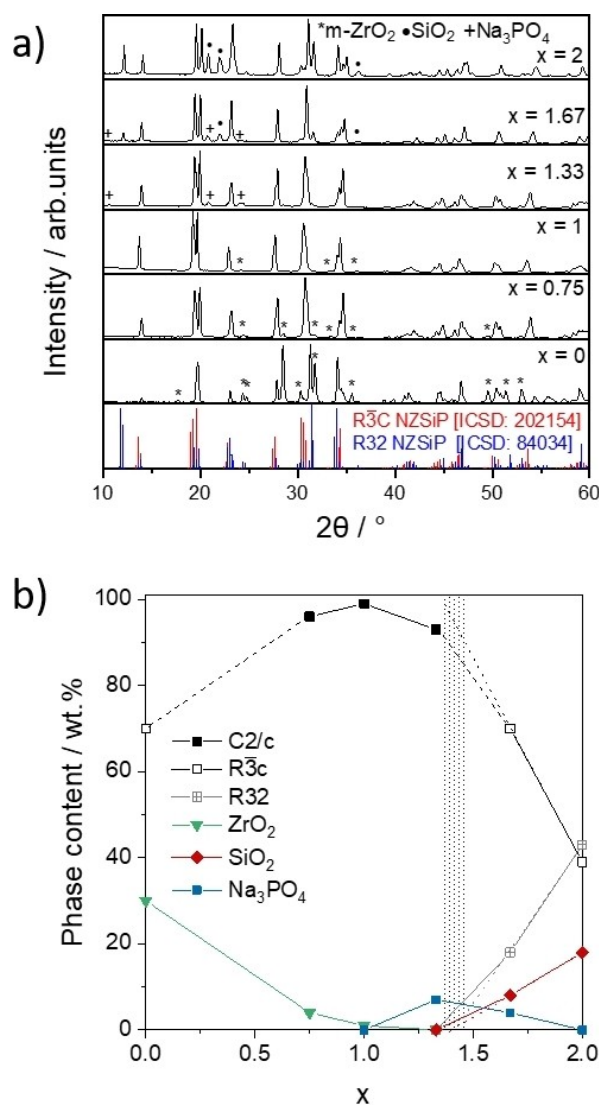
Figure 6. a) XRD patterns of $Na_3Zr_{3-x}Si_2P_xO_{11.5+x/2}$ with $0 \leq x \leq 2$ after sintering at 1370 °C ($x = 0$), 1250 °C ($x = 0.75$), 1240 °C ($x = 1$), 1230 °C ($x = 1.33$), 1160 °C ($x = 1.67$), 1060 °C ($x = 2$). b) Phase contents determined by Rietveld refinement. Combining the data points in a linear manner at high x values towards 0 and 100% (dotted lines) leads to a common end at $x = 1.4$–1.5, indicating the limit of the $C2/c$ phase region and marked with the vertical dotted region.

of monoclinic ZrO_2. From the Rietveld refinement, the amount of ZrO_2 content greatly decreased to 4 wt.% and 1 wt.% for $Na_3Zr_{2.25}Si_2P_{0.75}O_{11.87}$ and $Na_3Zr_2Si_2PO_{12}$, respectively. This persistent presence of ZrO_2 in the NaSICON materials was often reported earlier.[27–30] Here, monoclinic ZrO_2 was detected as the secondary phase with different amounts only for samples with a high content of Zr ($0 \leq x \leq 1$) and heat-treated at high temperatures (>1230 °C). As a result, $Na_3Zr_{1.67}Si_2P_{1.33}O_{12.17}$ formed as a 93% monoclinic NaSICON phase and was initially refined as $Na_3Zr_2Si_2PO_{12}$ (ICSD No. 202154), with 7% of Na_3PO_4 detected as an impurity. It was mentioned earlier that the sintering temperature of ~ 1200 °C is the most appropriate temperature to obtain the pure NaSICON phase.[25]

ChemPhysChem

Articles
doi.org/10.1002/cphc.202100032

**Chemistry
Europe**
European Chemical
Societies Publishing

$Na_3Zr_{1.33}Si_2P_{1.67}O_{12.33}$ and $Na_3ZrSi_2P_2O_{12.5}$ contained a phase mixture with an inhomogeneous distribution of Si so that two phases can be distinguished: a rhombohedral Si-rich phase with $R\bar{3}c$ symmetry refined as $Na_{3.35}Zr_2Si_2P_{0.65}O_{12}$ (ICSD No. 62386)[16] and a Si-poor phase with $R32$ symmetry refined as $Na_{5.28}Zr_{0.94}Si_{0.5}P_{2.5}O_{12}$ (ICSD No. 84034),[31] with a ratio of 68/18 wt.% and 44/37 wt.%, respectively. This observation was also noticed by Guin et al.[32] for $Na_{3.4}Sc_2Si_{0.4}P_{2.6}O_{12}$. Furthermore, 10 wt.% and 19 wt.% tridymite (SiO_2) with space group $P6_3/mmc$ (ICSD No. 40896)[33] was detected as a secondary phase in $Na_3Zr_{1.33}Si_2P_{1.67}O_{12.33}$ and $Na_3ZrSi_2P_2O_{12.5}$, respectively.

During refinement of the two latter compositions, the site occupancies initially were not restricted. This, however, resulted in insufficient charge neutrality for three of the four compositions. Therefore, for each composition, up to seven different compositions were defined to account for different charge compensation mechanisms. Then the defined compositions of the $R\bar{3}c$ and $R32$ phases were refined by permutation and by keeping the corresponding site occupancies constant. The quality of the refinements was evaluated on the basis of the R values (R_{wp}, $R_{Bragg}^{R\bar{3}c}$, R_{Bragg}^{R32}). In the case of $Na_3Zr_{1.33}Si_2P_{1.67}O_{12.33}$, 25 combinations were refined. Here, the first refinement, as mentioned before, already produced an electroneutral composition of $Na_{2.3}Zr_{1.76}Si_2PO_{11.17}$ for the $R\bar{3}c$ phase and remained the best solution of the refinements with the lowest R values in combination with compositions $Na_5ZrSi_{3-x}P_xO_{10.5+x/2}$ with $0 < x < 1$ for the $R32$ phase ($R_{wp} = 5.06–5.07$, $2.32 < R_{Bragg}^{R\bar{3}c} < 2.35$ and $2.18 < R_{Bragg}^{R32} < 2.34$). The final weight percentages were 70 wt.%, 18 wt.%, 8 wt.% and 4 wt.% for the $R\bar{3}c$ phase, the $R32$ phase, SiO_2 and Na_3PO_4, respectively.

Similarly, $Na_3ZrSi_2P_2O_{12.5}$ was refined with 35 combinations and four of these showed the lowest R values with $R_{wp} = 6.70–6.80$, $R_{Bragg}^{R\bar{3}c} = 2.70–2.73$, $R_{Bragg}^{R32} = 4.01–4.24$. These lowest R values were obtained for compositions with the general formula $Na_{1+x-y}Zr_{2-z}Si_xP_{3-x}O_{12-y/2-2z}$ and $x=2$, $y=0.8$ and $0.1 < z < 0.2$, resulting in a composition such as $Na_{2.2}Zr_{1.85}Si_2PO_{11.3}$ for the $R\bar{3}c$ phase. The $R32$ phase showed the lowest R values for $Na_{1+4y+2z}Zr_{2-y}Si_xP_{3-x}O_{12-x/2+z}$ with $x=0.5$, $1 < y < 1.05$ and $0 < z < 0.2$. A mean composition can be written as $Na_{5.2}Zr_{0.975}Si_{0.5}P_{2.5}O_{11.8}$. Here, the final refinements resulted in 39 wt.%, 43 wt.% and 18 wt.% for the $R\bar{3}c$ phase, the $R32$ phase and SiO_2, respectively.

Since $Na_3Zr_{1.33}Si_2P_{1.67}O_{12.33}$ and $Na_3ZrSi_2P_2O_{12.5}$ were sintered at a low temperature very close to the melting point, it may be possible that these temperatures are not appropriate to obtain a single NaSICON phase. Since the crystallization of the NaSICON phase requires a higher sintering temperature,[26] the two compounds may be regarded as poorly equilibrated.

In the case of $Na_3Si_2P_3O_{13}$, just before the melting point at 600 °C, no NaSICON structure was obtained. Instead, two phases formed: orthorhombic $Na_3P_3O_9$ with space group $Pmcn$ (ICSD No. 18139)[34] and SiO_2 with the trigonal α-quartz structure ($P3_221$) (ICSD No. 16331).[35] At a slightly higher temperature, towards the sharp length change (Figure 2) and with the DTA signal at about 620 °C (Figure 4), the sample became amorphous, but showed hardly any shrinkage (2.3%) during the sintering process just below the melting point. $Na_3P_3O_9$ has a low melting point below 650 °C[18,34] and its presence causes the

sample to melt. Hence, this composition is not discussed further in this paper.

In addition, all samples were sintered at a constant temperature for comparison (Figure 7). Here the $R\bar{3}c$ and the $R32$ phase also dominate the XRD patterns with varying phase contents and broader reflections than in Figure 6a. This indicates an imperfect phase formation and is supported by the presence of unreacted precursor materials. Monoclinic ZrO_2 with space group $P2_1/c$ was detected as a secondary phase in all specimens with $0 \leq x \leq 1.33$. Moreover, tridymite (SiO_2) was also identified but only for Si-rich materials ($1.67 \leq x \leq 2$).

2.4.2. Lattice Parameters

For the materials with $0.75 \leq x \leq 1.33$, a decrease of the monoclinic unit cell parameters a and b was observed, while an increase of the c lattice parameter was obtained with increasing phosphorous content (Table 4). For the samples with $x = 0$, 1.67 and 2 as a subgroup, the same trend was observed after conversion of the hexagonal lattice parameters to the monoclinic crystal system. The whole series then tends to show a continuous change of the unit cell parameters and the volume. In addition, the three data points for $0.75 \leq x \leq 1.33$ are very similar and indicate an intermediate plateau for all lattice parameters and hence a consistent monoclinic phase region. When $Na_3Zr_2Si_2PO_{12}$ is used as a reference, the lattice parameters $a = 15.67(1)$ Å, $b = 9.07(1)$ Å, $c = 9.21(1)$ Å and $\beta = 123.96(3)°$ are in good agreement with the literature.[9,20,25,30]

The unit cell volume decreases with increasing x as might be anticipated with the substitution of Zr^{4+} (0.72 Å) with P^{5+} (0.212 Å). Within the series, however, it should be kept in mind that the changing composition is not a substitution due to the different sites of the two cations, but rather the adjustment of phase equilibria determining the lattice parameters. For
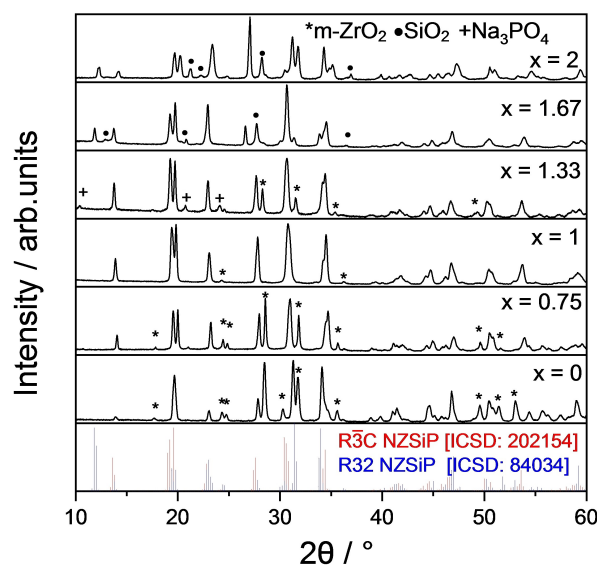

Figure 7. XRD patterns of $Na_3Zr_{3-x}Si_2P_xO_{11.5+x/2}$ with $0 \leq x \leq 2$ after sintering all specimens at 1000 °C.

ChemPhysChem

Articles
doi.org/10.1002/cphc.202100032

Chemistry
Europe
European Chemical
Societies Publishing

Table 4. Unit cell parameters and theoretical density of the $Na_3Zr_{3-x}Si_2P_xO_{11.5+x/2}$ samples. For the calculation of the theoretical density, the compositions $Na_4Zr_2Si_3O_{12}$ (x=0), $Na_3Zr_2Si_2PO_{12}$ (0.75 < x < 1.33), $Na_{2.3}Zr_{1.76}Si_2PO_{11.17}$ and $Na_5ZrSi_{2.5}P_{0.5}O_{10.75}$ (x=1.67), $Na_{2.2}Zr_{1.85}Si_2PO_{11.3}$ and $Na_{5.2}Zr_{0.975}Si_{0.5}P_{2.5}O_{11.8}$. (x=2) were used.

x	Space group	Content/wt.%	a_m/Å	b_m/Å	c_m/Å	β/°	V_m/Å³	a_{hex}/Å	c_{hex}/Å	V_{hex}/Å³	R_{wp}/%	$d_{theo.}$/ g cm^{-3}
0	R$\bar{3}$c	70	–	–	–	–	–	9.187(6)	22.22(1)	1624.4	7.3	3.38
0.75	C2/c	96	15.68(1)	9.073(9)	9.220(9)	123.90(6)	1088.69	–	–	–	5.69	3.25
1	C2/c	99	15.67(1)	9.070(1)	9.21(1)	123.96(3)	1086.81	–	–	–	4.83	3.24
1.33	C2/c	93	15.65(1)	9.054(9)	9.228(9)	123.74(6)	1087.9	–	–	–	5.75	3.24
1.67	R$\bar{3}$c	70	–	–	–	–	–	8.96(1)	22.91(3)	1596.0	5.19	2.99
	R32	18	–	–	–	–	–	9.16(3)	21.8(1)	1585.3		2.91
2	R$\bar{3}$c	39	–	–	–	–	–	8.92(1)	22.84(3)	1575.9	7.14	3.08
	R32	43	–	–	–	–	–	9.154(1)	21.84(3)	1583.2		3.07

comparison of the crystallographic parameters, the values of the series $Na_{4-x}Zr_2Si_{3-x}P_xO_{12}$ are included in Figure 8. Although the two series are aligned towards different – and in terms of
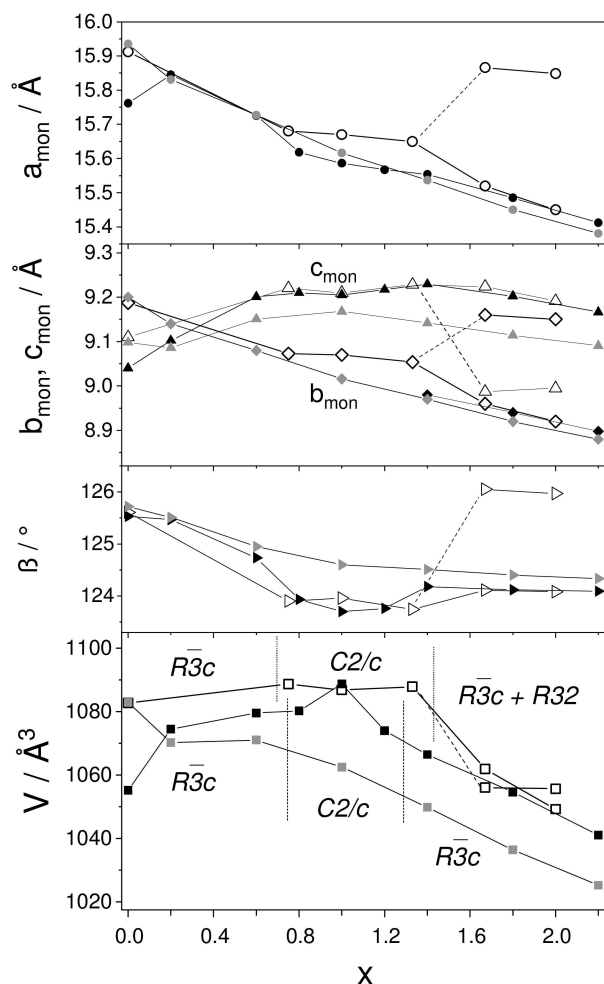
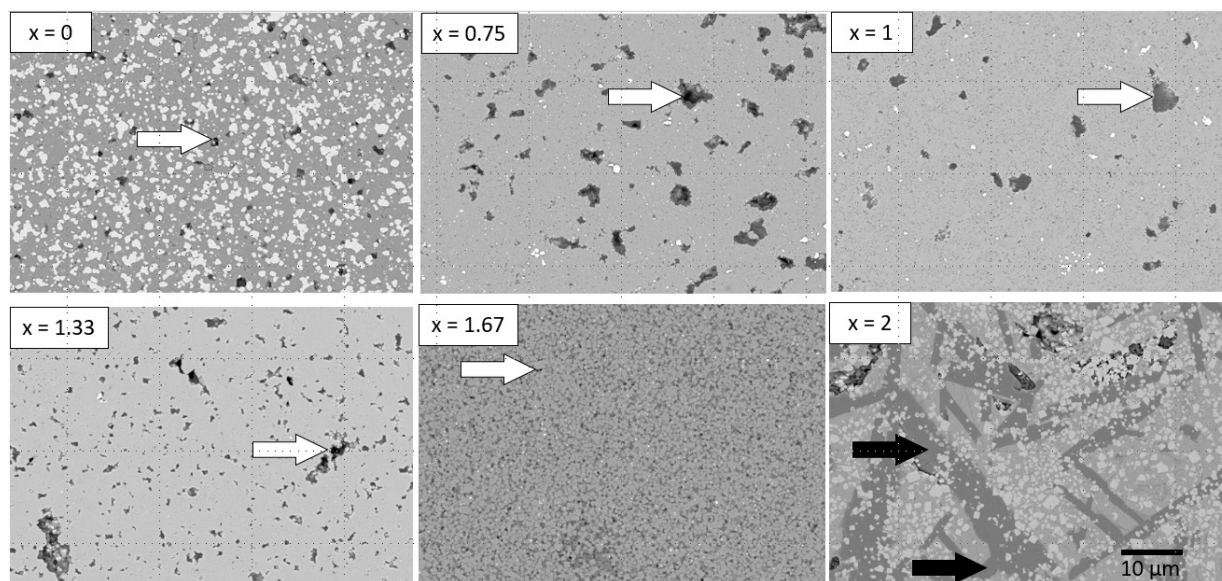**Figure 8.** Monoclinic lattice parameters and corresponding unit cell volume of the series $Na_3Zr_{3-x}Si_2P_xO_{11.5+x/2}$ with $0 \leq x \leq 2$. For comparison, the crystallographic data of the series $Na_{4-x}Zr_2Si_{3-x}P_xO_{12}$ are included (black symbols,[9] gray symbols[23]). The monoclinic phase regions for both series are tentatively indicated by dotted vertical lines. The lattice parameters of the converted R32 phase are linked with the other data points by the short-dashed lines.

the sodium content, nearly perpendicular – directions in the quaternary phase diagram, certain features show interesting similarities. Starting with $Na_3Zr_3Si_2O_{11.5}$, this composition seems to convert to $Na_4Zr_2Si_3O_{12}$ and ZrO_2 (see Figure 6). When the structure refinement of $Na_3Zr_3Si_2O_{11.5}$ was carried out with space group R$\bar{3}$c, the lattice parameters and cell volume resulted in values very close to $Na_4Zr_2Si_3O_{12}$ as reported by others.[9,22] The unit cell of $Na_3Zr_3Si_2O_{11.5}$ is slightly larger than in the previous studies, which is probably related to small differences in the stoichiometry (see Figure 5). For the following compositions and similarly to the series $Na_{4-x}Zr_2Si_{3-x}P_xO_{12}$, the NaSICON structure changes to the monoclinic phase ($\approx 0.35 < x < 1.45$ for $Na_3Zr_{3-x}Si_2P_xO_{11.5+x/2}$ assuming the same V_{hex} at which the phase change occurs for $Na_{4-x}Zr_2Si_{3-x}P_xO_{12}$ with $\approx 0.75 < x < \approx 1.25$). Within both series the NaSICON structure returns back to the rhombohedral phase and can be associated with compositions with smaller unit cell volumes. At x = 1.67, when the cell volume shows a pronounced reduction for the series $Na_3Zr_{3-x}Si_2P_xO_{11.5+x/2}$, the R32 phase also emerged as shown in Figure 8 by the two data points connected with dashed lines.

It is interesting to note that on the one hand the lattice parameters of the R$\bar{3}$c phase are in very good agreement with the series $Na_{4-x}Zr_2Si_{3-x}P_xO_{12}$.[9] On the other hand, the lattice parameters of the R32 phase fit very well with those of $Na_5ZrP_3O_{12}$[31,36] indicating the aforementioned phase separation in Si-rich and Si-poor compounds, respectively. It also implies that the sodium content is unequally distributed among the two rhombohedral phases and that a miscibility gap exists in the region of $1.4 < x < 2.0$ in $Na_3Zr_{3-x}Si_2P_xO_{11.5+x/2}$.

2.5. Microstructural Analysis

The SEM images of polished cross-sections of the sintered ceramics are shown in Figure 9. ZrO_2 was observed as a secondary phase with different concentrations in the samples with x = 0, 0.75 and 1. It can be clearly distinguished as white particles with different morphologies. Furthermore, the amount of ZrO_2 decreased with increasing x and disappeared for x = 1.33, 1.67 and 2, which is in good agreement with the XRD patterns. The microstructural analysis of the cross-section of $Na_3Zr_3Si_2O_{11.5}$ revealed an area fraction of 29.7 % for ZrO_2. This

ChemPhysChem

Articles
doi.org/10.1002/cphc.202100032

Chemistry Europe
European Chemical
Societies Publishing

Figure 9. SEM images of polished cross-sections of sintered $Na_3Zr_{3-x}Si_2P_xO_{11.5+x/2}$ ceramics. The sintering temperatures are listed in Table 1. In the top row, the white phase is ZrO_2. The black arrows show the SiO_2 phase and the white arrows indicate pores.

corresponds to about 42 wt.% ZrO_2 in a phase mixture with $Na_4Zr_2Si_3O_{12}$, which deviates from the XRD result by about 10 wt.%. The high amount of ZrO_2 in $Na_3Zr_3Si_2O_{11.5}$ can be better understood assuming the formation of $Na_4Zr_2Si_3O_{12}$ at high temperatures and the overall chemical reaction:

$$Na_3Zr_3Si_2O_{11.5} \rightarrow$$
$$2/3\ Na_4Zr_2Si_3O_{12} + 1/6\ Na_2ZrO_3 + 3/2\ ZrO_2 \quad (1)$$
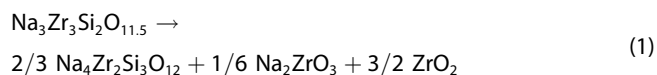
and accompanied by the decomposition of Na_2ZrO_3 due to the evaporation of sodium oxide:

$$Na_2ZrO_3 \rightarrow ZrO_2 + Na_2O \quad (2)$$

According to Reaction 1, the amount of ZrO_2 is 64 mol% and adding the ZrO_2 content from Reaction 2 results in 71 mol% ZrO_2 and 29 mol% $Na_4Zr_2Si_3O_{12}$. This phase mixture corresponds to 36 wt.% and 64 wt.% or 25 vol.% and 75 vol.%, respectively, which is close to the obtained experimental values. Since the impurity phase Na_2ZrO_3 was not detected by XRD, Reaction 2 is a realistic assumption.

When the sintering temperature was decreased from 1350 °C for $Na_3Zr_3Si_2O_{11.5}$ to 1250 °C and 1240 °C for $x = 0.75$ and 1, the concentration of ZrO_2 also decreased in the NaSICON phase materials to 4 wt.% and 1 wt.%, respectively. However, the high relative density of these samples of 94% and 96%, respectively, is not easily obtained, because below these temperatures no significant densification was obtained and at higher temperatures a volume expansion was observed either due to recrystallization or evaporation of volatile species, resulting in low density as shown in Figure 3. Therefore, the optimum sintering temperature range was very narrow because

of the partial melting point, which was very close to the optimal sintering temperature.

Apart from ZrO_2, the SEM images show that the grain sizes are homogeneous for all compositions, with the micron-sized grains appearing to be well sintered together and tightly connected to each other. In addition, almost no fractures or micro-cracks are observed. The densification of samples with $0 < x < 2$ is quite evident in the SEM images, while very little porosity is observed, which is in good agreement with the high relative density (see Table 1).

In the case of $x = 2$ the microstructure shows a dense sample composed of several phases. The energy-dispersive X-ray spectroscopy (EDX) analyses (not shown here) detected the presence of different phases with an inhomogeneous distribution of Si, with the result that two phases can be distinguished in good agreement with the Rietveld refinement: $Na_{2.2}Zr_{1.85}Si_2PO_{11.3}$, the Si-rich phase, contained more silicon and zirconium and less phosphorus, which can be distinguished in the SEM image as the brightest phase due to the highest average atomic number. The Si-poor phase with less silicon and zirconium and more phosphorus ($Na_{5.2}Zr_{0.975}Si_{0.5}P_{2.5}O_{11.8}$) appears as a medium shade of gray. The SiO_2 can also be seen as a dark gray phase. An adequate presence of Na_3PO_4 could not be observed either in cross-sectional images or in the XRD patterns. For $x = 1.67$, the microstructure shows the existence of a phase mixture with very small particles. The light gray phase contained more silicon and zirconium than the dark gray phase. A quantitative analysis of the individual phases was not possible due to the electron beam sensitivity of the materials.

ChemPhysChem

Articles
doi.org/10.1002/cphc.202100032

**Chemistry
Europe**

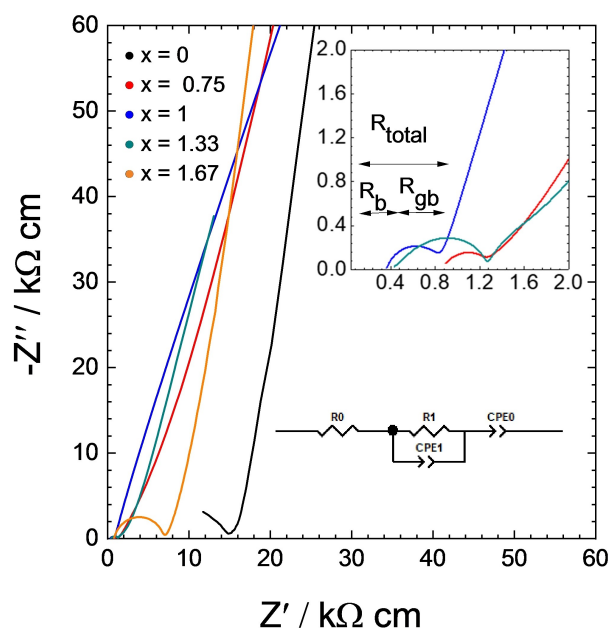European Chemical
Societies Publishing

2.6. Electrical Conductivity

In order to compare the electrical conductivity within the series of compositions, impedance spectra were measured at 25 °C and the Nyquist plots of $Na_3Zr_{3-x}Si_2P_xO_{11.5+x/2}$ with $0 \leq x \leq 1.67$ are shown in Figure 10. Only one depressed semicircle that does not begin at the origin can be observed among all samples at high frequencies. This indicates that the deconvolution of grain (R_b) and grain boundary (R_{gb}) resistances is possible assuming that the high-frequency intercept with the x-axis corresponds to the grain (bulk) resistance. The semicircle is the response of the grain boundary resistance and the low-frequency intercept with the x-axis is the total resistance ($R_t = R_b + R_{gb}$) of the sample. The straight line at low frequencies is due to the electrode polarization. The radius of the semicircle decreases with increasing x until x=1 and then increases until x=1.67. Hence the sample with x=1 shows the smallest R_t within the series.

The bulk and total conductivity of the samples were calculated with Equation 1

$$\sigma = \frac{L}{A\,R} \tag{1}$$

where L and A represent the pellet thickness and electrode surface area of the specimen, respectively, and R is either R_b or R_t deduced from the fitted impedance spectra.
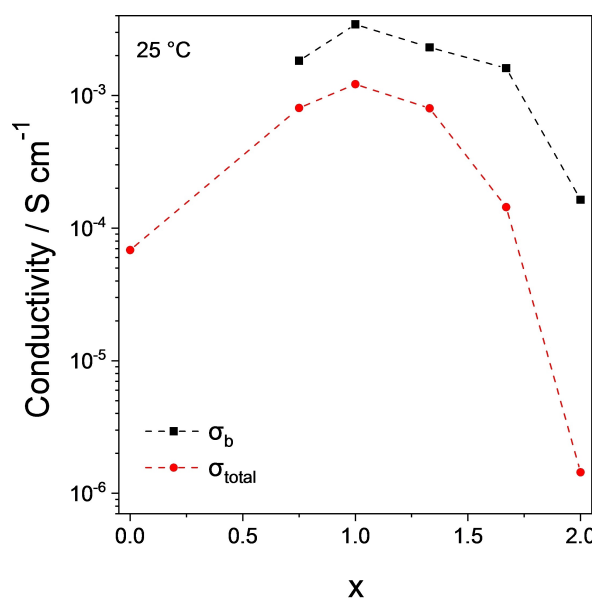
2.6.1. Total Conductivity

The total ionic conductivity at 25 °C for $Na_3Zr_3Si_2O_{11.5}$ is 6.83×10^{-5} S cm^{-1}. This low value can be related to the low sodium concentration in the material caused by its evaporation at a high processing temperature, which in turn leads to the formation of a higher amount of ZrO_2. In addition, the resulting NaSICON composition, $Na_4Zr_2Si_3O_{12}$ or small deviations from it, contains only a very limited number of sodium vacancies leading to poor ionic conductivity.[21]

The increasing amount of P_2O_5 in the ceramics increases the total ionic conductivity and reaches a maximum value of 1.22×10^{-3} S cm^{-1} for $Na_3Zr_2Si_2PO_{12}$ (Figure 11). This value is in very good agreement with previous studies for the same composition (1.2×10^{-3} S cm^{-1}[37] and 1×10^{-3} S cm^{-1}[38]) using conventional solid-state reaction (SSR) and solution-assisted SSR (SA-SSR), respectively. Further increase of P_2O_5 again results in the reduction of the total ionic conductivity by one order of magnitude for the compositions $Na_3Zr_{1.67}Si_2P_{1.33}O_{12.17}$ and $Na_3Zr_{1.33}Si_2P_{1.67}O_{12.33}$. Furthermore, the P-rich material $Na_3ZrSi_2P_2O_{12.5}$ shows a very low ionic conductivity for several reasons: the large unit cell volume, the presence of a phase mixture and the increasing occurrence of secondary phases as observed from the microstructure and confirmed by the XRD pattern. In addition, the poorer density of 90% results in an ionic conductivity at 25 °C that is two to three orders of magnitude lower than for the three compositions with a monoclinic NaSICON structure. Processing, structural and microstructural factors are regarded as reasons for the low conductivity of $Na_3ZrSi_2P_2O_{12.5}$ as well as $Na_3Zr_3Si_2O_{11.5}$.

Figure 10. Nyquist plot of impedance spectra at 25 °C of $Na_3Zr_{3-x}Si_2P_xO_{11.5+x/2}$ with $0 \leq x \leq 1.67$ after accounting for the sample dimensions. The inset shows the magnification of the high frequency region. The resistance contributions in the inset refer to the blue line. The equivalent circuit is also shown.

Figure 11. Bulk and total conductivity at 25 °C as a function of x in $Na_3Zr_{3-x}Si_2P_xO_{11.5+x/2}$.

2.6.2. Bulk Conductivity

The bulk conductivity (σ_b) is calculated by normalizing the R_b value to the sample dimensions according to Equation (1). This resistance is obtained by fitting the impedance spectra with an equivalent circuit as shown in Figure 10 and extracting the lowest value of $-Z''$ on the left side of the semi-circle as the bulk resistance R_b. The equivalent circuit for fitting consists of pure resistances (R0 and R1) and constant phase elements (CPE0 and CPE1). The constant phase elements (CPE) represent the non-ideal capacitive contributions of the transport processes in the bulk (CPE_b), at the grain boundaries (CPE_{gb}) and at the electrode/electrolyte interface at low frequencies (CPE_{el}). The CPE is described by a capacitance value (C_{CPE}) and an exponent n usually varying between 1 and 0.5. If n equals 1, then the equation is indistinguishable from that of a capacitor. If n equals 0.5, a 45° line is formed on the complex plane graph. When a CPE is connected in parallel to a resistance, a Cole element (depressed semi-circle) is obtained in the graph. The C_{CPE} is associated with the capacitance C as written in Equation (2). The capacitance values depend on the shape and size of the semi-circle.[39]

$$C = R^{\frac{1-n}{n}} \, C_{CPE}^{\frac{1}{n}} \qquad (2)$$

For $x=0$, only half of the semicircle appears and does not allow a precise determination of R_b.

The bulk and total conductivity at 25 °C is plotted as a function of x in Figure 11. The highest bulk conductivity value of 3.44×10^{-3} S cm^{-1} was observed for $Na_3Zr_2Si_2PO_{12}$. In general, the total conductivity is highest when the unit cell volume is smallest (cf. Figure 8 and Figure 11). If the unit cell volume increases, the conductivity is lowered. This variation seems to be related to the structural change between monoclinic and rhombohedral crystal symmetry. Bulk conductivity for all compositions roughly follows the similar trend of the total ionic conductivity. Accordingly, bulk conductivity drops in correlation with structural factors that include crystal symmetry and the lattice parameters. Therefore, materials crystallizing with $R\bar{3}c$ crystal symmetry show lower bulk conductivity than those with $C2/c$ symmetry.[39–41] The site occupancy of Na in the reference NaSICON material, $Na_3Zr_2Si_2PO_{12}$, is 75% and there are three Na sites in the formula unit, namely Na(1), Na(2) and Na(3).[42] The Na(1) sites are thermodynamically more stable compared to the other two. Consequently, it is likely that these sites will be preferentially filled with the Na$^+$ ions. The remaining Na$^+$ ions are then randomly dispersed between the available Na(2) and Na(3) sites. Samples with the monoclinic NaSICON structure show higher ionic conductivity because the sodium conduction occurs along two pathways, Na(1) – Na(2) – Na(1) and Na(1) – Na(3) – Na(1). Based on density-functional theory (DFT) computations,[20] they differ in the bottleneck area between the Na(1) sites. In contrast, the rhombohedral crystal structure has only two sites for sodium occupancy and the Na$^+$ ions hop from the Na(1) to the Na(2) site along only one pathway.[43] Since only the monoclinic materials show higher ionic con-

ductivity, this pathway variation might be the reason for such a large difference in the bulk conductivity.

2.6.3. Activation Energy

The activation energy E_a of the ionic conductivity of all compounds except $x=3$ was obtained from impedance measurements at different temperatures and using the Arrhenius law (Equation 3), where σ_t is the total conductivity at the absolute temperature T, A is a pre-exponential constant containing the number of charge carriers, jump distance and attempt frequency[44,45] and k is the Boltzmann constant.

$$\sigma_T T = A \, e^{\frac{-E_a}{kT}} \qquad (3)$$

The activation energy values were calculated from the slope of ln σ_tT versus inverse temperature in the temperature range of -20 °C to 60 °C as shown in Figure 12. The calculated values of E_a after linear fitting are summarized in Table 5. A scatter in activation energy of the $Na_3Zr_{3-x}Si_2P_xO_{11.5+x/2}$ specimens was observed, varying between 0.285 eV and 0.565 eV without any clear trend. The conductivity is highest for $Na_3Zr_2Si_2PO_{12}$ in the temperature range of 0 °C to 60 °C with an E_a of 0.359 eV, which

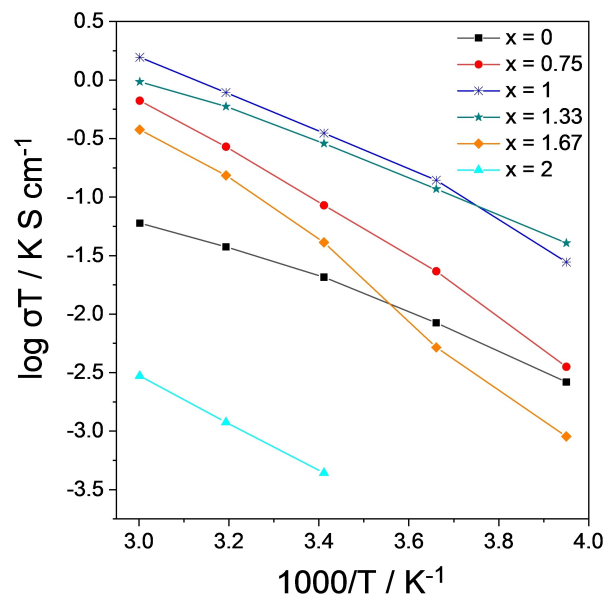**Figure 12.** Arrhenius plot of σ_t of $Na_3Zr_{3-x}Si_2P_xO_{11.5+x/2}$ measured in the temperature range of -20 °C to 60 °C.

Table 5. Bulk and total conductivity at 25 °C and activation energy values of total conductivity of $Na_3Zr_{3-x}Si_2P_xO_{11.5+x/2}$.

x	σ_b / S cm^{-1}	σ_t / S cm^{-1}	$E_a(\sigma_t)$ / eV	Temperature range / °C
0	–	6.83×10^{-5}	0.285 ± 0.016	-20–60
0.75	1.83×10^{-3}	8.06×10^{-4}	0.473 ± 0.017	-20–60
1	3.44×10^{-3}	1.22×10^{-3}	0.359 ± 0.021	-20–60
1.33	2.31×10^{-3}	8.01×10^{-4}	0.292 ± 0.010	-20–60
1.67	1.61×10^{-3}	1.44×10^{-4}	0.565 ± 0.026	-20–60
2	1.64×10^{-4}	1.44×10^{-6}	0.401 ± 0.004	20–60

ChemPhysChem

Articles
doi.org/10.1002/cphc.202100032

Chemistry
Europe
European Chemical
Societies Publishing

is very similar to the reported values for the same material, e.g. $E_a = 0.352$ eV prepared by the Pechini method,[38] 0.361 eV by SA-SSR[38] and 0.380 eV by a sol-gel route.[46] Different temperature ranges and small stoichiometric variations may explain the slight differences.

Figure 11 shows that the bulk and total conductivity at 25°C for the two compounds $Na_3Zr_{1.33}Si_2P_{1.67}O_{12.33}$ and $Na_3ZrSi_2P_2O_{12.5}$ tend to be lower compared to the other compositions with $0.75 \leq x \leq 1.33$. The major differences between these materials mostly result from crystallographic factors: the increased P^{5+} content leads to the formation of two rhombohedral symmetries with larger unit cell volume than the samples with a monoclinic structure. The existence of mixed rhombohedral phases and the increased presence of SiO_2 are responsible for the increase in resistance and an enhanced blocking of charge carriers.[47]

In the case of $Na_3ZrSi_2P_2O_{12.5}$ the conductivity is about two orders of magnitude lower than that of $Na_3Zr_{1.33}Si_2P_{1.67}O_{12.33}$. It is assumed that the conductivity is dominated by the $R32$ phase, which forms a continuous path in the phase mixture (see Figure 9), whereas the $R\bar{3}c$ phase shows disconnected, individual particles that do not contribute to the long-range ionic conduction. At elevated temperatures, however, it seems that this phase is thermally activated, and ions may transfer across the $R32/R\bar{3}c$ phase boundaries, leading to measurable conductivity.

3. Conclusions

The series $Na_3Zr_{3-x}Si_2P_xO_{11.5+x/2}$ was synthesized by the SA-SSR method. Rietveld refinement of the XRD patterns revealed that the phase region of NaSICON materials in the quaternary phase diagram $Na_2O–SiO_2–ZrO_2–P_2O_5$ is larger than expected. $Na_3Zr_3Si_2O_{11.5}$ predominantly crystallizes with a rhombohedral NaSICON structure with composition $Na_4Zr_2Si_3O_{12}$ together with significant amounts of monoclinic ZrO_2. Unexpectedly, the composition with $x = 0.75$ also belongs to compositions with a monoclinic NaSICON structure. The samples crystallizing with space group $C2/c$ ($0.75 \leq x \leq 1.33$) show higher ionic conductivity compared to the other samples crystallizing with rhombohedral symmetry. According to the crystallographic and microstructural results, the phase region of NaSICON can be enlarged as shown in Figure 13.

It turned out that the ionic conductivity depends on processing, structural and microstructural conditions: a) From the processing point of view, the sintering temperature decreased when the phosphorus content increased, especially when $x > 1.5$. The reason behind this trend is the glass phase formation on the Si- and P-rich side of the quaternary phase diagram. The advantage of reducing the processing temperature by raising the phosphate content was accompanied by decreasing ionic conductivity. b) The processing route determines the microstructure and has a direct influence on the density. Moreover, the presence of mixed NaSICON phases in the P-rich materials may contribute to the low ionic conductivity. The phase mixture can be described as an inhomogeneous distribution of both silicon and sodium and as the result of demixed NaSICONs with different compositions. c) In the case of the crystal structure, the unit cell volume shows a distinct plateau for the compounds crystallizing with monoclinic symmetry. The general trend of the unit cell volume directly influences the ionic (bulk) conductivity, showing the highest conductivity in this compositional region. Increasing the
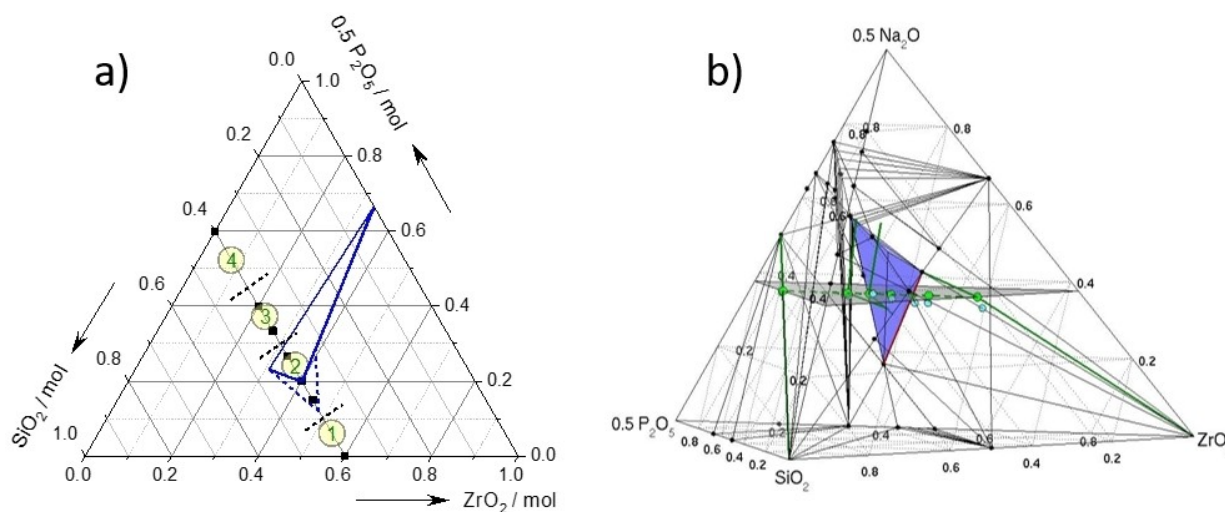
Figure 13. a) Intersection of the quaternary phase diagram at the constant molar fraction of sodium of $\xi_{Na} = 0.375$ with the obtained tentative phase regions of the series $Na_3Zr_{3-x}Si_2P_xO_{11.5+x/2}$: ① $Na_4Zr_2Si_3O_{12}$ ($R\bar{3}c$) + ZrO_2, ② $Na_3Zr_{3-x}Si_2P_xO_{11.5+x/2}$ ($C2/c$) with $\approx 0.75 < x \approx 1.45$, ③ $Na_{1+x-y}Zr_{2-z}Si_xP_{3-x}O_{12-y/2-2z}$ ($R\bar{3}c$) with $x = 2$, $0.5 < y < 0.8$ and $0.1 < z < 0.25$ as well as $Na_{1+4y+2z}Zr_{2-y}Si_xP_{3-x}O_{12-x/2+z}$ ($R32$) with $x \approx 0.5$, $1 < y < 1.05$ and $0 < z < 0.2$ as well as SiO_2. ④ $Na_{1+4y+2z}Zr_{2-y}Si_xP_{3-x}O_{12-x/2+z}$ ($R32$), SiO_2 and $Na_3P_3O_9$. The NaSICON phase region (blue triangle) can be extended for the area enclosed by the blue dashed lines. The products formed in regions ①, ③ and ④ are incorrectly represented, because they appear above and below the shown triangle with $\xi_{Na} = 0.375$. In b) the quaternary phase diagram shows the stability region of NaSICON (blue), the solid solution $Na_{4-x}Zr_2Si_{3-x}P_xO_{12}$ (red line), the nominal compositions (green circles), the analytical compositions (light blue circles), the phases in equilibrium and the compositions formed after sintering (green lines).

ChemPhysChem

Articles
doi.org/10.1002/cphc.202100032

Chemistry Europe
European Chemical
Societies Publishing

amount of ZrO_2 and SiO_2 as the secondary phase has an additional undesirable impact on the ionic conductivity even if the ceramics can be prepared with high density.

Therefore, it can be concluded that ionic conductivity increases with increasing P_2O_5 content to a maximum in the order of $10^{-3}\,S\,cm^{-1}$ at $x = 1$. Further increase of P_2O_5 changes the crystal structure to rhombohedral symmetry, increases the tendency of phase separation and the amount of impurity phases and decreases the densification and total ionic conductivity.

Experimental Section

Different powders within the series $Na_3Zr_{3-x}Si_2P_xO_{11.5+x/2}$ with $0 \leq x \leq 3$ were synthesized by the solution-assisted solid state reaction (SA-SSR) as described elsewhere.[38] Stoichiometric quantities of high purity Na_2CO_3 (Alfa Aesar, 99.5%), ZrO_2 (Saint-Gobain, 99.8%) and SiO_2 (Alfa Aesar, 99.8%) were mixed in a quartz glass container using water with 5% nitric acid to obtain a homogeneous aqueous suspension, to which the corresponding amount of $NH_4H_2PO_4$ was then added while stirring. The whole mixture was stirred overnight with 300 rpm at 70 °C for slow evaporation of the water. Then the homogenized mixture was heated from 70 °C up to 100 °C and the dried solid mixture was annealed in an oven at 600 °C for 5 h to form an amorphous raw powder. Afterwards the product was calcined at 900 °C for 5 h except for the sample with $x = 3$. The calcined powder was then ground in an agate mortar and finally milled in ethanol with zirconia balls (5 mm and 3 mm) on a roller bench for 48 h at 200 rpm. Differential thermal analysis/thermogravimetry (DTA/TG) measurements were carried out on the calcined powders up to 1500 °C in air with heating and cooling rates of 300 K/h using the simultaneous thermal analyzer STA449F1 Jupiter coupled to the QMS 403 C Aëolos mass spectrometer from NETZSCH-Gerätebau GmbH. The dilatometry experiments were performed with a 402 C dilatometer (also from NETZSCH-Gerätebau GmbH) applying a heating rate of 300 K/h. During the measurement, the shrinkage was recorded until a shrinkage of 25% was reached.

The powders were pressed into pellets (diameter = 13 mm, thickness ~2 mm) applying a pressure of about 150 MPa followed by sintering in Pt crucibles. The sintering temperatures were adjusted to the composition and were derived from the shrinkage curves in the dilatometer measurements. After sintering, the experimental density was obtained using the weight and volume of the pellets and the theoretical density was derived from the X-ray diffraction (XRD) refinement results.

The sintering process and melt formation were also measured with a thermo-optical device (TOMMI plus, Fraunhofer ISC, Germany). It combines a high temperature oven with an optical dilatometer. The silhouette of the sample is recorded by a CMOS camera. The device is controlled by a standard computer and operated using a graphical user interface. Besides the data acquisition on dimensional changes, single images as well as time-lapsed videos of the thermal treatment can be recorded.

Before and after sintering of the calcined powders, the stoichiometry of the specimens was checked by inductively coupled plasma optical emission spectroscopy (ICP-OES) using a Thermo Scientific iCAP7600 spectrometer with optical scale and CID semi-conductor detector, axial and radial reflection, and wavelengths between 166 nm and 847 nm. 50 mg of calcined powder was mixed with 0.5 g of lithium borate in a platinum crucible and fired for 1 hour at 1000 °C in a muffle furnace. The liquefied material was dissolved in 30 mL HCl (5%). After dissolution, the sample solutions were transferred to sample vials containing 0.5 mL of HF and filled to a volume of 50 mL volume. This measurement was performed twice for each composition.

The sintered specimens were characterized with respect to their crystal structure and phase purity using XRD measurements from $2\theta = 10°$ to $80°$ with a step size of $0.02°$ and a scan time of 0.75 s/step. The measurements were recorded with a Bruker D4 Endeavor diffractometer using Cu K_α radiation. The Rietveld refinements of the collected XRD data were performed using the TOPAS V.4.2 (Bruker AXS 2008, Karlsruhe, Germany) computer software. The microstructure of the polished cross-sections of the sintered pellets was examined by scanning electron microscopy (SEM, Ultra55, Zeiss).

The surfaces of prepared dense pellets were dry polished using SiC sandpapers up to a grit of 4000 and then sputter-coated with gold on each side to act as blocking electrodes using a Cressington 108 coater. The ionic conductivity was measured at different temperatures by an AC impedance analyzer system (Biologic, VMP-300) applying a frequency range from 7 MHz to 1 Hz. The resulting impedance spectra were fitted using the software "Z-view" (Scribner Associates Inc). The powders and pellets were stored in an argon-filled glove box until used later for further investigations.

Conflict of Interest

The authors declare no conflict of interest.

Keywords: NaSICON · ionic conductivity · solid electrolytes · sodium batteries · quaternary phase diagrams

[1] L. Joerissen, J. Garche, C. H. Fabjan, G. Tomazic, *J. Power Sources* **2004**, *127*, 98–104.
[2] D. Larcher, J.-M. Tarascon, *Nat. Chem.* **2015**, *7*, 19–29.
[3] H. Pan, Y. S. Hu, L. Chen, *Energy Environ. Sci.* **2013**, *6*, 2338–2360.
[4] R. Benato, N. Cosciani, G. Crugnola, S. D. Sessa, G. Lodi, C. Parmeggiani, M. Todeschini, *J. Power Sources* **2015**, *293*, 127–136.
[5] G. J. May, A. Hooper, *J. Mater. Sci.* **1978**, *13*, 1480–1486.
[6] E. Yi, E. Temeche, R. M. Laine, *J. Mater. Chem. A* **2018**, *6*, 12411–12419.
[7] M. E. Brownfield, E. Foord, S. J. Sutley, T. Botinelly, *Am. Mineral.* **1993**, *78*, 653–656.
[8] J. B. Goodenough, H.-Y. P. Hong, J. Kafalas, *Mater. Res. Bull.* **1976**, *11*, 203–220.
[9] H.-Y. P. Hong, *Mater. Res. Bull.* **1976**, 11, 173–182.
[10] Q. Ma, C.-L. Tsai, X. K. Wei, M. Heggen, F. Tietz, J. T. S. Irvine, *J. Mater. Chem. A* **2019**, *7*, 7766–7776.

ChemPhysChem

Articles
doi.org/10.1002/cphc.202100032

Chemistry Europe
European Chemical
Societies Publishing

[11] a) K. Hayashi, K. Shima, F. Sugiyama, *J. Electrochem. Soc.* **2013**, *160*, A1467-A1472; b) Y. Noguchi, E. Kobayashi, L. S. Plashnitsa, S. Okadab, J.-i. Yamaki, *Electrochim. Acta* **2013**, *101*, 59–65; c) J. K. Kim, F. Mueller, H. Kim, D. Bresser, J. S. Park, D. H. Lim, G. T. Kim, S. Passerini, Y. Kim, *NPG Asia Mater.* **2014**, *6*, e144; d) B.-R. Kim, G. Jeong, A. Kim, Y. Kim, M. G. Kim, H. Kim, Y.-J. Kim, *Adv. Energy Mater.* **2016**, *6*, 1600862; e) L. Liu, X. Qi, Q. Ma, X. Rong, Y.-S. Hu, Z. Zhou, H. Li, X. Huang, L. Chen, *ACS Appl. Mater. Interfaces* **2016**, *8*, 32631–32636; f) Y. Lu, J. A. Alonso, Q. Yi, L. Lu, Z. L. Wang, C. Sun, *Adv. Energy Mater.* **2019**, *9*, 1901205; g) T. Lan, C.-L. Tsai, F. Tietz, X. K. Wei, M. Heggen, R. Dunin-Borkowski, R. Wang, Y. Xiao, Q. Ma, O. Guillon, *Nano Energy* **2019**, *65*, 104040; h) H. Yamauchi, J. Ikejiri, F. Sato, H. Oshita, T. Honma, T. Komatsu, *J. Am. Ceram. Soc.* **2019**, *102*, 6658–6667; i) X. Zhan, M. E. Bowden, X. Lu, J. F. Bonnett, T. Lemmon, D. M. Reed, V. L. Sprenkle, G. Li, *Adv. Energy Mater.* **2020**, *10*, 1903472; j) X. Zhan, J. F. Bonnett, M. H. Engelhard, D. M. Reed, V. L. Sprenkle, G. Li, *Adv. Energy Mater.* **2020**, *10*, 2001378.

[12] F. Tietz, *AIMS Mater. Sci.* **2017**, *4*, 1305–1318.

[13] U. von Alpen, M. F. Bell, H. Höfer, *Solid State Ionics* **1981**, *3–4*, 215–218.

[14] W. Vielstich, *Battery Development in Europe, Electrochemistry in Industry*, Springer, **1982**, pp. 181–193.

[15] P. Colomban, *Solid State Ionics* **1986**, *21*, 97–115.

[16] J. P. Boilot, G. Collin, P. Colomban, *J. Solid State Chem.* **1988**, *73*, 160–171.

[17] J. P. Boilot, G. Collin, P. Colomban, *Mater. Res. Bull.* **1987**, *22*, 669–676.

[18] E. Turkdogan, *Iron Steel Inst. London* **1952**, *172*, 1–15.

[19] S. Naqash, F. Tietz, E. Yazhenskikh, M. Müller, O. Guillon, *Solid State Ionics* **2019**, *336*, 57–66.

[20] H. Park, K. Jung, M. Nezafati, C. S. Kim, B. Kang, *ACS Appl. Mater. Interfaces* **2016**, *8*, 27814–27824.

[21] W. Baur, J. R. Dygas, D. H. Whitmore, J. Faber, *Solid State Ionics* **1986**, *18–19*, 935–943.

[22] D. Tran Qui, J. J. Capponi, J. C. Joubert, R. D. Shannon, *J. Solid State Chem.* **1981**, *39*, 219–229.

[23] R. E. Hann, P. R. Suitch, J. L. Pentecost, *J. Am. Ceram. Soc.* **1985**, *68*, C285–C286.

[24] R. O. Fuentes, F. M. Figueiredo, F. M. B. Marques, J. L. Franco, *J. Eur. Ceram. Soc.* **2001**, *21*, 737–743.

[25] P. K. Jha, O. P. Pandey, K. Singh, *Silicon* **2017**, *9*, 411–419.

[26] R. S. Gordon, G. R. Miller, B. J. McEntire, E. D. Beck, J. R. Rasmussen, *Solid State Ionics* **1981**, *3–4*, 243–248.

[27] J. P. Boilot, J. P. Salanie, G. Desplanches, D. Le Potier, *Mater. Res. Bull.* **1979**, *14*, 1469–1477.

[28] M. L. Bayard, G. Barna, *J. Electroanal. Chem.* **1978**, *91*, 201–209.

[29] A. Ignaszak, P. Pasierb, R. Gajerski, S. Komornicki, *Thermochim. Acta* **2005**, *426*, 7–14.

[30] F. Lalère, J. B. Leriche, M. Courty, S. Boulineau, V. Viallet, C. Masquelier, V. Seznec, *J. Power Sources* **2014**, *247*, 975–980.

[31] J. P. Boilot, G. Collin, R. Comes, *Solid State Ionics* **1983**, *9–10*, 829–833.

[32] M. Guin, E. Dashjav, C. M. N. Kumar, F. Tietz, O. Guillon, *Solid State Sci.* **2017**, *67*, 30–36.

[33] K. Kihara, T. Matsumoto, M. Imamura, *Z. Krist. – Cryst. Mater.* **1986**, *177*, 39–52.

[34] H. Ondik, *Acta Crystallogr.* **1965**, *18*, 226–232.

[35] H. d'Amour, W. Denner, H. Schulz, *Acta Crystallogr. Sect. B* **1979**, *35*, 550–555.

[36] J. P. Boilot, G. Collin, R. Comes, *J. Solid State Chem.* **1983**, *50*, 91–99.

[37] K. Hayashi, K. Shima, F. Sugiyama, *J. Electrochem. Soc.* **2013**, *160*, A1467-A1472.

[38] S. Naqash, Q. Ma, F. Tietz, O. Guillon, *Solid State Ionics* **2017**, *302*, 83–91.

[39] S. Naqash, D. Sebold, F. Tietz, O. Guillon, *J. Am. Ceram. Soc.* **2019**, *102*, 1057–1070.

[40] M. Guin, F. Tietz, O. Guillon, *Solid State Ionics* **2016**, *293*, 18–26.

[41] E. R. Losilla, M. A. G. Aranda, S. Bruque, M. A. Paris, J. Sanz, A. R. West, *Chem. Mater.* **1998**, *10*, 665–673.

[42] E. M. Vogel, R. J. Cava, E. Rietman, *Solid State Ionics* **1984**, *14*, 1–6.

[43] S. Naqash, F. Tietz, O. Guillon, *Solid State Ionics* **2018**, *319*, 13–21.

[44] A. R. West, *Solid state chemistry and its applications*, John Wiley & Sons, 2nd edition, **2014**.

[45] J. B. Goodenough, *Annu. Rev. Mater. Res.* **2003**, *33*, 91–128.

[46] H. Khireddine, P. Fabry, A. Caneiro, B. Bochu, *Sens. Actuators B* **1997**, *40*, 223–230.

[47] O. Bohnke, S. Ronchetti, D. Mazza, *Solid State Ionics* **1999**, *122*, 127–136.